Emergence of net magnetization by magnetic field biased diffusion in antiferromagnetic $L1_0$ NiMn

Nicolas Josten [1,*] Sakia Noorzayee,[2] Olga Miroshkina [1] Benjamin Zingsem [1] Mehmet Acet [1] Ulf Wiedwald,[1]
Aslı Çakır [3] Markus E. Gruner [1] and Michael Farle [1]

[1]*Faculty of Physics and Center for Nanointegration (CENIDE), University of Duisburg–Essen, Duisburg 47057, Germany*
[2]*Chair for Materials Science and Engineering, Ruhr University Bochum, Universitätsstrasse 150, 44780 Bochum, Germany*
[3]*Department of Metallurgical and Materials Engineering, Muğla Sıtkı Koçman University, 48000 Muğla, Turkey*

NiMn is a collinear antiferromagnet with high magnetocrystalline anisotropy ($K = -9.7 \times 10^5$ J m^{-3}). Through magnetic annealing of NiMn with excess Ni, strongly pinned magnetic moments emerge due to an imbalance in the distribution of Ni in the antiferromagnetic Mn sublattices. The results are explained with a model of magnetic field biased diffusion, supported by *ab initio* calculations. Another observation is the oxidation of Mn at the surface, causing an enrichment of Ni in the subsurface region. This leads to an additional ferromagnetic response appearing in the magnetization measurements, which can be removed by surface polishing.

I. INTRODUCTION

Collinear antiferromagnets are characterized by an antiparallel alignment of neighboring magnetic moments resulting in a net magnetization of zero. Applying a magnetic field can have no effect, can result in canting of the moments in the field direction, or can induce a spin-flop or spin-flip transition depending on the orientation and strength of the antiferromagnetic (AF) anisotropy. Net magnetic moments in antiferromagnets can also develop when there are defects in the crystal. This can be the case for surfaces [1], interfaces [2], impurities [3,4], vacancies [5], and chemical disorder [6].

NiMn is a tetragonal $L1_0$ intermetallic antiferromagnet below 1000 K and a cubic B2 paramagnet above this temperature. The Néel temperature is estimated to be about 1070 K [7], which lies above the $L1_0$ stability-range. NiMn has a strong magnetocrystalline anisotropy ($K = -9.7 \times 10^5$ J m^{-3}) [8] and has been used as a pinning layer for exchange bias applications in films [9].

When NiMn has a slight excess in Ni, uncompensated moments and ferromagnetic (FM) interactions can appear in the predominantly AF matrix and modify the magnetic properties such as those observed in Ref. [10]. The authors annealed a sample of NiMn with 54.9 at.% Ni at different temperatures between 750 and 790 K for 20 h in 1 T. This led to the appearance of uncompensated moments due to biased diffusion of Ni-excess atoms within the Mn AF sublattices. They determined an activation energy of 1.8 eV typical for an atomic diffusion process. They also encountered the emergence of an isotropic magnetization, which they attributed to inhomogeneities containing excess Ni within the sample.

Uncompensated magnetic moments in antiferromagnets are of special interest for the understanding of exchange bias [11,12]. A linear dependence between the amount of pinned moments and the strength of the exchange bias field was shown in Ref. [13]. Therefore, controlling the amount of uncompensated moments would be necessary to optimize the exchange bias effect.

Here, we examine the formation of strongly pinned magnetic moments after annealing Ni$_{51.6}$Mn$_{48.4}$ in a magnetic field. For such a study, we stress the importance of inhomogeneities considered in Ref. [10], and we develop a method to control them and to eliminate their influence on the actual observation of pinned moments. We then extend the magnetic field biased diffusion model used in [10] to describe the origin of the strong directional pinning and perform *ab initio* calculations for supportive evidence.

II. EQUIATOMIC NiMn AND THE CONSEQUENCES OF EXCESS Ni

Around the equiatomic concentration, NiMn exhibits three crystallographic phases with changing temperature [14]. The high-temperature A1 phase is face-centered cubic (fcc). Below $\sim$1200 K it forms an ordered B2 lattice (CsCl). Then, below the martensitic transition [15] at $\sim$1000 K, the tetragonal $L1_0$ (CuAu) phase stabilizes, where NiMn is an antiferromagnet.

We show in Fig. 1 the crystal- and spin-structure of $L1_0$ NiMn and the consequences of excess Ni. In Fig. 1(a), dashed lines show the $L1_0$ unit cell with $P4/mmm$ space group. The structure can also be considered as a cell shown with solid lines. This cell is described with the $C4/mmm$ space group commonly referred to as "face-centered tetragonal". The
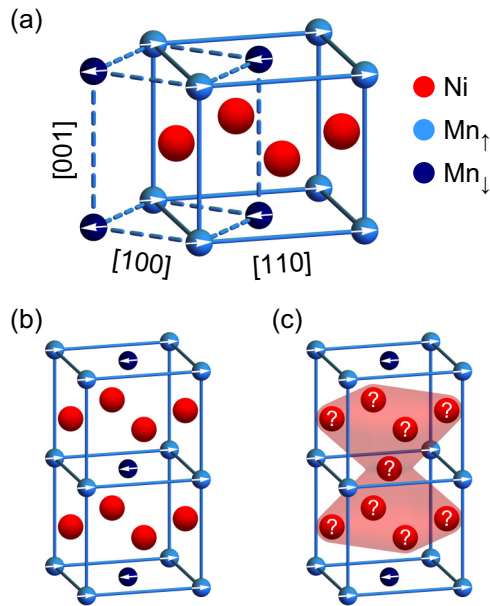
---

*Nicolas.Josten@uni-due.de

FIG. 1. (a) Crystal- and spin-structure of $L1_0$ NiMn. The arrows indicate the direction of the magnetic moments. The Ni-moment is essentially zero. (b) The $L1_0$ NiMn crystal structure with two "face-centered tetragonal" cells on top of each other. (c) The same structure as (b), but with the Mn-atom at the center substituted by a Ni-atom. This leads to the formation of a nine-atom Ni-cluster shaded in red. The question marks indicate the unknown magnetic moments in this configuration.

directions of the magnetic moments are indicated by arrows. Neutron diffraction studies show that the magnetic easy-axis lies within the basal plane. However, it cannot differentiate between the [100] and [110] directions [16]. These studies provide a magnetic moment of $4\mu_B$ per Mn atom and essentially no magnetic moment for Ni with an upper bound of $0.2\mu_B$ [7,16]. *Ab initio* calculations [8] provide evidence in favor of [110] as the easy axis and a magnetic moment between $3\mu_B$ and $4\mu_B$ while Ni has no moment [8,17]. The results of spin-polarized scanning tunneling microscopy studies show also that the moments point along the [110] direction at the surface of NiMn films grown on Cu(001) [18]. In this work, we adopt the easy-axis as the [110] direction, although it would have been just as valid if the [100] direction was adopted as the easy-axis.

Figure 1(b) shows the NiMn crystal structure with two "face-centered tetragonal" cells on top of each other. If excess Ni up to 6% (above which NiMn becomes fcc) is introduced, some Ni atoms have to occupy Mn sites. This leads to the formation of Ni clusters with at least nine atoms, as depicted in Fig. 1(c). The question marks indicate the unknown magnetic moments in this configuration.

III. METHODS

A. Experimental

NiMn with excess Ni was prepared by arc melting pure elements ($\geqslant$99.98%) and subsequent homogenization for 5 days at 1223 K with the sample encapsulated in a quartz tube under Ar atmosphere. Afterwards, it was quenched in water

at room temperature. We polished the surface of this sample and determined, with energy-dispersive x-ray spectroscopy (EDX) incorporated in a scanning electron microscope, the composition to be $Ni_{51.6}Mn_{48.4}$. Afterwards, the sample was cut into cuboids and a disk using a precision sectioning saw, while subsequent polishing removed any residues from the surface.

X-ray diffraction (XRD) measurements using Cu $K\alpha$ radiation were carried out on the disk. The disk was then annealed again in a quartz tube with Ar for 6 h at 650 K for additional XRD measurements with and without polishing the surface.

The magnetic properties of two cuboids were measured in a vibrating sample magnetometer (VSM) using a Quantum Design PPMS DynaCool. For magnetic annealing, the samples were mounted on a Quantum Design VSM Oven Heater-Stick using ceramic-based Zircar cement. On the first sample, an initial state $M(B)$-curve was measured in $\pm$ 9 T at 326 K. Magnetic annealing was done for 14.4 h at 650 K in five steps in a field of 9 T, where after each step, the $M(B)$-curve was measured at 326 K. After the last step, the surface was polished to remove any surface corrosion, and again the $M(B)$-curve was measured. The second cuboid was annealed for 2.9 h at 650 K without a magnetic field. Afterwards, a temperature-dependent magnetization curve at 10 mT was measured with a speed of 4 K min^{-1} between 326 and 907 K. Then, this sample was used for x-ray photoemission spectroscopy (XPS) depth profiling to determine the chemical state and stoichiometry variations as a function of depth using a ULVAC-PHI VersaProbe II with monochromatized Al $K\alpha$ radiation. Depth profiling was done by Ar$^+$ sputtering initially at 1 kV down to a depth of about 25 nm. It was then sputtered at 3 kV for various times leading to a total sputtered thickness of (720 ± 30) nm. The thickness was calibrated using the calibration of thermally grown SiO$_2$ on Si substrates.

B. *Ab initio* calculations

First-principles calculations were performed with two approaches for chemical disorder modeling. The first one is the coherent potential approximation (CPA) realized in spin-polarized relativistic Korringa-Kohn-Rostoker (SPR-KKR) code [19,20]. The second one is a supercell approach realized in the Vienna *Ab Initio* Simulation Package (VASP) [21,22]. For both VASP and SPR-KKR calculations, the exchange-correlation functional was treated within the generalized gradient approximation (GGA) following the Perdew, Burke, and Ernzerhof (PBE) scheme [23]. A detailed description of computational parameters can be found in Appendix.

We perform first noncollinear CPA calculations for [001], [100], and [110] spin moment directions to determine the energetically favorable configuration. Further, it also allows us to evaluate the magnetocrystalline anisotropy energy (MAE) (see Appendix). In all cases, Mn magnetic moments have a so-called layered antiparallel orientation [16,24,25] which is known to be the most energetically favorable and provides zero total magnetization of NiMn. It was shown that the [110] spin moment direction is energetically the most favorable among the considered cases. The magnitudes of the magnetic moments are very similar for all three orientations. Results of CPA calculations are presented in Appendix. For the mod-

eling of disorder in the supercell approach, we performed collinear calculations to save computational costs. Within this approach, we modeled a 432-atom supercell by repeating a 16-atom cell three times along each of the Cartesian axes. We considered equiatomic NiMn and a structure where one Mn atom in the middle of the supercell [(0.5; 0.5; 0.5) site] is substituted by a Ni-excess-atom. For these systems, we performed structural relaxation and determined the total and site-resolved magnetic moments.

IV. RESULTS

A. Structure

We show the XRD results in Fig. 2. The data were refined using JANA2006 [26]. Figure 2(a) shows the XRD-data of the disk-sample in the initial state. Two phases are observed. The first is the tetragonal $L1_0$ phase of NiMn, and the second is MnO. The lattice parameters we obtain for the $L1_0$ phase are $a = (2.63 \pm 0.01)$ Å and $c = (3.54 \pm 0.01)$ Å, and for MnO $a = (4.44 \pm 0.01)$ Å, which are in agreement with Refs. [27,28]. The XRD-data after an additional heat-treatment of 6 h at 650 K are seen in Fig. 2(b). The amount of MnO increases, and an additional fcc phase appears. For the refinement, we assume an A1 phase and obtain a lattice parameter of $a = (3.55 \pm 0.01)$ Å. This falls in the range of lattice parameters corresponding to stoichiometries between $Ni_{56}Mn_{44}$ and Ni ($a = 3.52$ Å [29]). After additional polishing of the surface, no trace of the additional Ni-rich phase is left, and the amount of MnO decreases as shown in Fig. 2(c). MnO is present in all three states of the sample. Its amount in the initial state and the annealed and polished state is small compared to the unpolished annealed state. It most likely stems from residual oxygen during arc melting. EDX measurements on all three states of the disk provide a similar amount of Ni and Mn. This means the thickness of the MnO and Ni-rich phase is smaller than the sampling depth of EDX. The EDX measurements on the annealed disk additionally show the presence of oxygen.

B. Magnetization

To be able to study the effects of magnetic field biased diffusion, first, surface and volume effects contributing to the magnetization have to be separated. Surface effects are largely eliminated by polishing the sample as mentioned in Sec. III A. However, this should be verified, especially by examining in detail the surface effects themselves. We study the magnetization of initial-state (as-prepared), annealed samples, and annealed surface-treated samples to be able to account for the pinning properties occurring within the volume of the sample.

We show in Fig. 3 $M(B)$ data for $Ni_{51.6}Mn_{48.4}$ measured first in the initial state, then after consecutive annealing steps at 650 K in a field of -9 T, and finally for the polished sample, as mentioned in Sec. III A. Figure 3(a) shows $M(B)$ in our full measurement range $-9 < B < 9$ T. Here, a typical behavior for an antiferromagnet can be observed with a slight nonlinearity at high fields. The deviation from linearity observed as of about 3 T is related to spins being forced to rotate towards the field direction. In this scale, the curves for all measurements overlap. However, zooming into the low-field region,
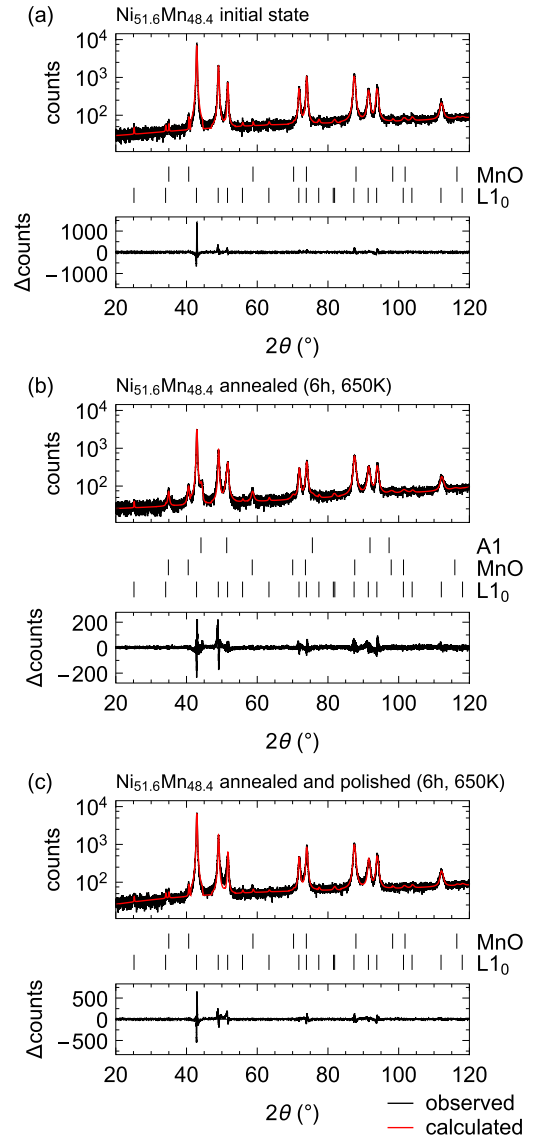

FIG. 2. Refined room-temperature XRD measurements of the bulk NiMn sample. The Δcounts are the difference between the observed and calculated curves. (a) XRD measurement done directly after quenching the sample from 1223 K in room-temperature water. (b) XRD measurement after an annealing treatment of 6 h at 650 K. (c) XRD-measurement after additional surface polishing after the annealing treatment.

as shown in Fig. 3(b), reveals features for each measurement. Two main features can be observed. First, while in the initial state the $M(B)$-curve crosses the origin with no hysteresis, it develops a hysteresis essentially broadening in the vertical direction with increasing annealing time, as per measurement protocol indicated in the figure. Secondly, a vertical shift of the loops occurs. This shift remains constant even after reversing the field, meaning that the involved magnetic moments are strongly pinned. When the sample surface is polished, the hysteresis is eliminated, but the vertical shift remains.

The saturation magnetization of the hysteresis loop M_{hyst} can be obtained by subtracting the linear response to $M(B)$, which comes from the AF component, and the size of the
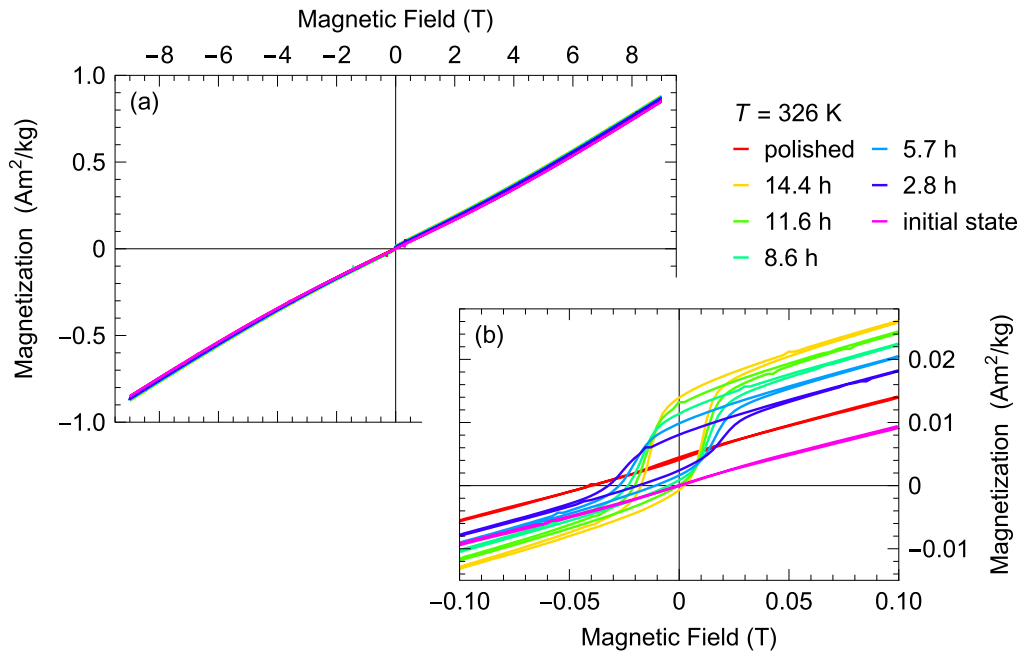
FIG. 3. (a) Field-dependent magnetization curves of $Ni_{51.6}Mn_{48.4}$ measured at 326 K before and after magnetic annealing for various times at 650 K and 9 T. A slight nonlinearity can be observed at high fields for both measurements. (b) The region around zero field in more detail. After annealing, the $M(B)$-curve is shifted upwards along the magnetization axis, which is referred to as a vertical shift. Additionally, a hysteresis emerges, which can be eliminated by polishing the sample surface.

vertical shift M_{shift}. An offset signal arising from the heater-stick of 0.95×10^{-3} A m^2/kg was also subtracted from the saturation magnetization.

Figure 4 shows the annealing-time dependence of M_{shift} and M_{hyst} along with the effect of surface polishing. Both M_{shift} and M_{hyst} increase with progressive annealing. While M_{shift} saturates gradually, M_{hyst} increases constantly after the first annealing step. After polishing the sample surface, M_{hyst}

vanishes while M_{shift} decreases by 35% as seen by the open symbols. This means that the origin of M_{hyst} is related only to the surface, while M_{shift} originates from the bulk.

We now compare the $M(B)$ of the initial and polished states. For this, we plot in Fig. 5 the respective $M(B)$ curves from Fig. 3. Here the emerging vertical shift in $M(B)$ has a value of $M_{shift} = (4.3 \pm 0.7) \times 10^{-3}$ A m^2/kg. All other feature in the $M(B)$ curves are identical.

To understand the reasons behind the hysteresis occurring due to surface effects, another sample was annealed for 2.9 h at 650 K with no magnetic field applied. No vertical shift occurs in $M(B)$ in this case [10]. This is confirmed in Fig. 6(a),
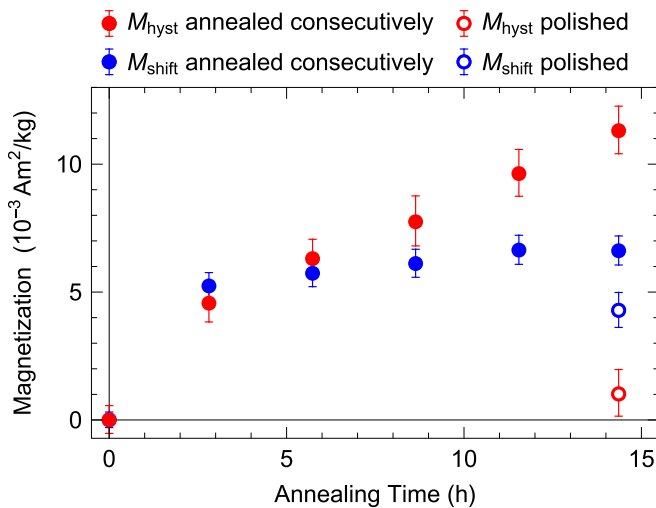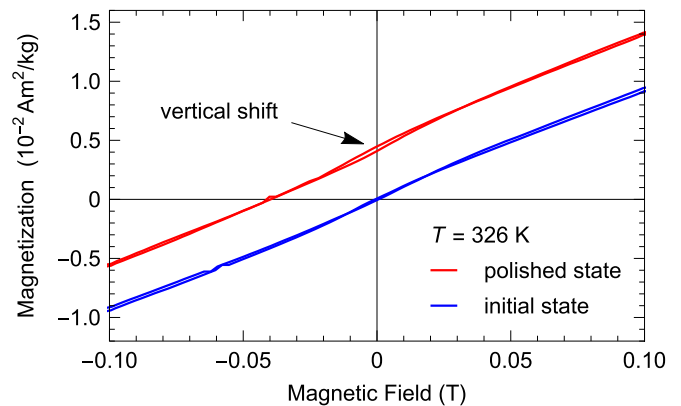

FIG. 4. Annealing time-dependent vertical shift and saturation magnetization of the hysteresis after magnetic annealing for various times at 650 K and 9 T. After the final annealing treatment, the sample surface was polished and then remeasured. While the saturation magnetization vanishes, the vertical shift is decreased by 35%.

FIG. 5. Field-dependent magnetization measurements of $Ni_{51.6}Mn_{48.4}$ around zero field measured at 326 K in the initial state and after magnetic annealing for 14.4 h at 650 K and 9 T and subsequent surface polishing.
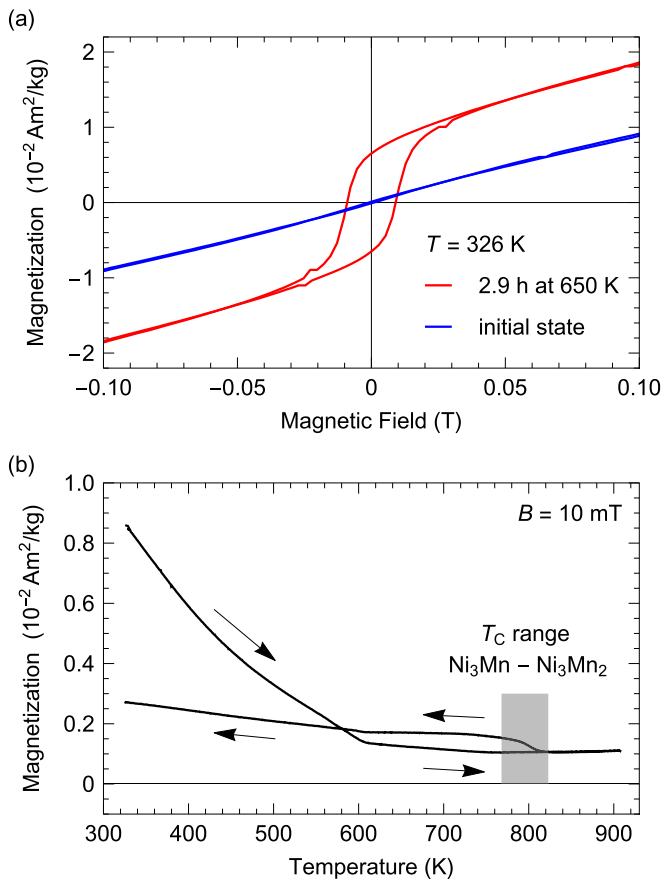
(a)

(b)

FIG. 6. (a) Field-dependent magnetization curves of $Ni_{51.6}Mn_{48.4}$ measured at 326 K before and after annealing without an applied magnetic field for 2.9 h at 650 K. Here only the emerging hysteresis is visible without any vertical shift. (b) Temperature-dependent magnetization of the same sample measured after annealing between 326 and 907 K at 10 mT. The magnetization declines constantly with increasing temperature until around 600 K. While sweeping up, no distinct Curie temperature is visible. After coming back down from 907 K, a Curie temperature around 800 K appears, which matches Curie temperatures observed in stoichiometries between Ni_3Mn_2 and Ni_3Mn.

which shows the $M(B)$ curves of this sample measured before and after annealing. The hysteresis, on the other hand, is still present after annealing. The total magnetization of this hysteresis deviates from the total magnetization of the hysteresis shown in Fig. 3. Except for the applied magnetic field, both samples were subject to comparable annealing procedures. Unlike volume effects, surface effects can vary in their mass magnetization. This is because differences in size and shape of the samples can change the surface-to-volume ratio. After annealing, we performed a temperature-dependent magnetization measurement under 10 mT between 326 and 907 K. The sample was not polished in between. The small field of 10 mT does not lead to any substantial preferred-orientation pinning. We show the results in Fig. 6(b). While sweeping the temperature upwards, a gradual decrease of magnetization is present up to 600 K. The reason for this is that the surface becomes FM when the Ni content exceeds 60% [30]. The Curie temperature T_C is strongly dependent on the stoichiometry and

degree of chemical order and varies between 300 and 820 K. The presence of different concentrations could therefore produce a gradual decrease in $M(T)$. $M(T)$ runs flat from 600 K up to the maximum temperature of 907 K. When sweeping down, a sharp increase in $M(T)$ occurs around 800 K, which corresponds to the T_C range observed for compositions between ordered Ni_3Mn_2 and Ni_3Mn. This feature, which is absent in the increasing-temperature data, may be caused by homogenization and chemical ordering at the sample surface. The curve remains temperature-independent down to about 600 K, below which it slowly increases. This corresponds to the end of the gradual decrease in $M(T)$ when measuring on increasing temperature.

C. X-ray photoemission spectroscopy

To fully understand the processes occurring at the surface, we have carried out depth resolved XPS on the sample used for the experiments plotted in Fig. 6. Figure 7 shows the results of XPS depth profiling.

Sputtering was carried out for 70 min with 1 kV Ar^+ ions and then at 3 kV for 220 min. Below 190 min this was done in intervals of 10 min and above in intervals of 50 min. Full spectra up to 1200 eV were taken in the unsputtered state (initial state), and after sputtering times of 50 min (intermediate state) and 290 min (final state). They are shown in Fig. 7(a). In the initial state, the survey spectrum shows Mn, O, and C but no Ni suggesting a significant oxidation of Mn at the surface and some C surface contaminants. The intermediate state is equivalent to about 25 nm sputtered thickness. C is sputtered away and is thus not present in the volume. Mn and O XPS signals strengthen while that of Ni begins to emerge. In the final state, after long-term sputtering of about 700 nm sputter depth, only Mn- and Ni-related signals are present while no O is detected proving that only the metallic state is present in the volume.

The full transition from an almost Ni-free Mn oxide surface towards a metallic alloy deep in the bulk with varying stoichiometry has been tracked by the XPS $2p$ core-level states. Figure 7(b) presents these spectra for the initial, intermediate, and final states. For Ni-$2p$ levels, it is clear that almost no Ni can be detected in the initial and intermediate states, but a fully metallic spectrum is present in the bulk after long-time sputtering. For Mn, the intensity of $2p$ levels increases after sputtering without changing the energy position. Mn is fully oxidized in the intermediate state, while long-term sputtering decreases the core level energies by about 3 eV, which corresponds to a Mn metallic signal. Note that the pronounced shoulder in the Mn-$2p_{3/2}$ originates from a Ni Auger peak.

Thus, we measured the relative line intensities on the Ni- and Mn-$2p_{1/2}$ peaks and determined their relative stoichiometry as shown in Fig. 7(c). After about 100 min sputtering time, the Ni-response sharply increases corresponding to an initial depth of about 130 nm. Within the next 60 nm, the Ni signal strongly rises up to 82 at. % relative to Mn and decreases gradually to about 75 at. % to the final state. Overall, the surface oxidation of the bulk $Ni_{51.6}Mn_{48.4}$ sample results in an almost Ni-free Mn oxide layer of about 130 nm and a Ni-rich metallic subsurface region. The thickness of this transition layer can
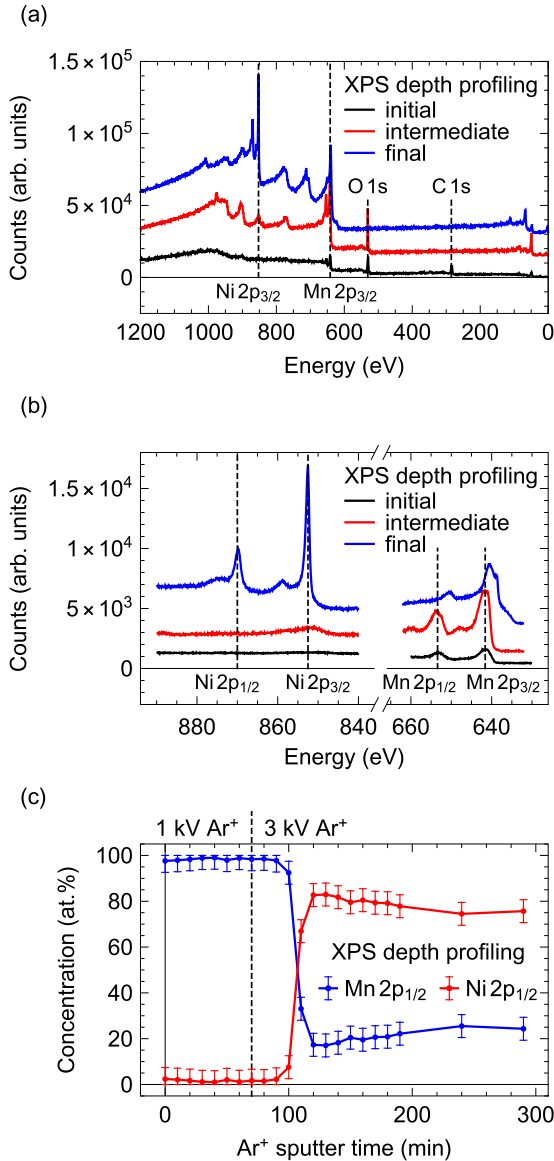
FIG. 7. XPS depth profiling of a bulk piece of $Ni_{51.6}Mn_{48.4}$ using Al $K\alpha$ radiation after annealing for 2.9 h at 650 K without applied field and subsequent sweep from 326 to 907 K and back at a rate of 4 K min^{-1}. Survey spectra (a) and Ni-$2p$ and Mn-$2p$ core-level spectra (b) in initial state and after sputtering with 1 kV Ar$^+$ ion for 50 min (intermediate) and after 290 min sputter time with 1 and 3 kV Ar$^+$ ions. (c) Relative concentrations of Ni and Mn determined from their $2p_{1/2}$ states nonoverlapping with Auger peaks from the other element.

be estimated to be about 2–3 μm by extrapolating the Ni- and Mn-content to be the volume-stoichiometry of $Ni_{51.6}Mn_{48.4}$. This Ni-rich metallic subsurface region is responsible for the hysteresis contribution seen in Fig. 3. This also explains why it can be removed by surface polishing.

D. Results of *ab initio* calculations

By *ab initio* calculations, we determined how a Ni-excess atom in the Mn-plane modifies the magnetic properties. Calculated site-resolved and total magnetic moments for ideal

NiMn and NiMn with one Mn-atom substituted by Ni are presented in Table I. The cells can be found in Figs. 8(a) and 8(b). When one substitutes one Mn-atom by Ni, the magnetization changes significantly in the vicinity of this defect. The Ni-excess-atom (Ni$_1$ in Fig. 8) itself acquires a moment of $\mu^{Ni_1} = 0.73\mu_B$/atom oriented parallel to the magnetic moments of the closest Mn atoms in the plane (Mn$_6$ in Fig. 8 with $\mu^{Mn_6} = 3.22\mu_B$/atom). The eight regular Ni atoms (Ni$_2$ in Fig. 8) surrounding the defect also acquire small magnetic moments of $0.09\mu_B$/atom. As a result, the layered AF configuration is no longer compensated, and the structure as a whole has a net moment above zero. In total, one Ni substitution generates, also including the polarization cloud involving the nearest Ni neighbors, a total magnetic moment of $5\mu_B$.

E. Biased diffusion

Next, we calculate the total pinned magnetization assuming a biased diffusion of defects in single-crystalline and polycrystalline antiferromagnets after magnetic annealing. We start with

$$\omega = \Gamma_0 \exp\left(-\frac{A}{k_B T_a}\right) \qquad (1)$$

as a simple model for the diffusive jump rate ω of an atom inside a crystal lattice [31,32]. Γ_0 is the attempt frequency, A is the activation energy, k_B is the Boltzmann constant, and T_a is the annealing temperature. In the presented case of NiMn, we concentrate on the diffusion of Ni-excess atoms within the Mn-plane. A sketch of this diffusion is given in Fig. 9. The position of a Ni-excess-atom in the Mn-plane is highlighted. In the Mn-plane, the magnetic moments of neighboring Mn-atoms point in opposite directions. As demonstrated by our *ab initio* calculations (see Sec. IV D), the direction of the magnetic moment of an excess Ni-atom points parallel to the magnetic moments of its Mn-neighbors. A swap of position with a Mn-neighbor therefore inverts the direction of this magnetic moment. This is demonstrated in Fig. 9(b) for a simplified case in which the magnetic field and the easy axis of the antiferromagnet coincide. Therefore, the activation energy for the jump of a Ni-excess-atom can be written as

$$A = A_0 - \vec{\mu} \cdot \vec{B}_a. \qquad (2)$$

Here $\vec{\mu}$ is the effective magnetic moment, which is present at the location of the Ni-excess atom occupying a Mn-site after the diffusive jump. This moment depends on the mechanism of diffusion and does not need to be the same as the moment in Table I, which we call $\vec{\mu}_{Total}$. This is the case, since $\vec{\mu}_{Total}$ represents the moment of a defect-free lattice (except for the Ni-excess atom), while different diffusion mechanisms rely on lattice defects, like vacancies. $\vec{B}_a$ is the applied magnetic field during annealing, and A_0 is the activation energy in zero field.

The Mn-plane of NiMn consists of two magnetic sublattices. This means that there only exist two possible states for Ni-excess atoms. The total number of Ni-excess atoms in the state where the Zeeman energy is minimized is N_-, while the number of excess atoms in the state with maximized Zeeman energy is N_+. The respective induced magnetic moments per excess atom are $\vec{\mu}_-$ and $\vec{\mu}_+$, so that $\vec{\mu}_- = -\vec{\mu}_+$. Since atoms
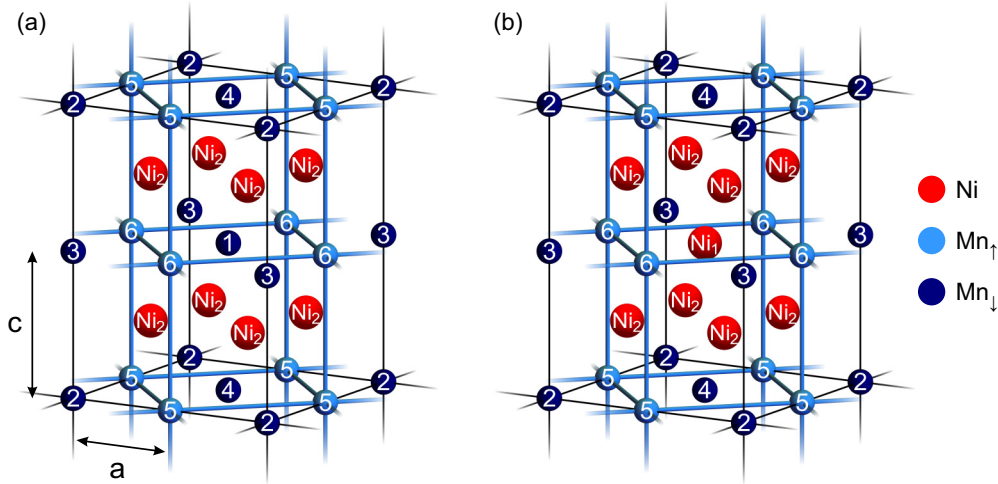
FIG. 8. (a) Equiatomic NiMn and (b) structure where the Mn-atom in the center was replaced by a Ni-atom (Ni_1). This leads to the emergence of a nonzero net magnetic moment. Supercells for the first-principles calculations are formed by a $3 \times 3 \times 3$ elongation of the 16-atom cell.

can always switch from one state to the other, this can be treated the same way as a reversible reaction in chemistry. The reaction rates are ω_- and ω_+ and their activation energies A_- and A_+. The rates are defined as

$$N_- \underset{\omega_+}{\overset{\omega_-}{\rightleftharpoons}} N_+. \tag{3}$$

If $\vec{\mu} \perp \vec{B}$, it follows that $\omega_- = \omega_+$. The jump rates can be written as

$$\omega_\pm = \Gamma_0 \exp\left(-\frac{\left(A_0 \mp \vec{\mu}_- \cdot \vec{B}_a\right)}{k_B T_a}\right). \tag{4}$$

Here the angle between $\vec{\mu}_-$ and $\vec{B}_a$ can only take values between 0 and $\frac{\pi}{2}$ since $\vec{B}_a$ defines the direction of $\vec{\mu}_-$. The condition for equilibrium during magnetic annealing is

$$N_- \omega_- = N_+ \omega_+. \tag{5}$$

This can be used to calculate the moment-, field-, and temperature-dependent ratio $\tilde{N}$ (also called the equilibrium constant) of the occupations N_- and N_+ as

$$\tilde{N} = \frac{N_-}{N_+} = \exp\left(\frac{2\,\vec{\mu}_- \cdot \vec{B}_a}{k_B T_a}\right). \tag{6}$$

Both the activation energy A_0 and the attempt frequency Γ_0 cancel out on division of the rates. $N = N_- + N_+$ is the total number of Ni-excess atoms. $\Delta N = N_- - N_+$ is their difference. From the ratio $\tilde{N}$, one can calculate the relative amount

of both N_- and N_+ and the relative imbalance between N_- and N_+ given by the equations

$$\frac{N_-}{N} = \frac{\tilde{N}}{\tilde{N}+1}, \tag{7a}$$

$$\frac{N_+}{N} = \frac{1}{\tilde{N}+1}, \quad \text{and} \tag{7b}$$

$$\frac{\Delta N}{N} = \frac{\tilde{N}-1}{\tilde{N}+1}. \tag{7c}$$

With the atomic mass as m_{Ni} and m_{Mn} and the atomic concentrations as c_{Ni} and c_{Mn}, one can also calculate the mass magnetization M_{shift} of the pinned magnetization using the equations

$$C = \frac{1}{2}\frac{c_{Ni} - c_{Mn}}{c_{Ni}m_{Ni} + c_{Mn}m_{Mn}} \quad \text{and} \tag{8}$$

$$M_{shift} = C\frac{\tilde{N}-1}{\tilde{N}+1}\,\vec{\mu}_{Total} \cdot \hat{e}$$

$$= C \tanh\left(\frac{\vec{\mu}_- \cdot \vec{B}_a}{k_B T_a}\right)\vec{\mu}_{Total} \cdot \hat{e}. \tag{9}$$

Here, C is a scale factor to achieve the correct percentage/mass-ratio, and $\hat{e}$ is a unit vector in the measurement direction. The dependence on tanh in Eq. (9) is the thermal equilibrium result of a two-state system. It can, for example, be found in spin-1/2 paramagnetism [33].

TABLE I. Site-resolved (in μ_B/atom) and total (in μ_B/Ni substitution) magnetic moments μ of the ideal equiatomic NiMn and NiMn with one Ni-excess atom. Numbering of atoms corresponds to Fig. 8.

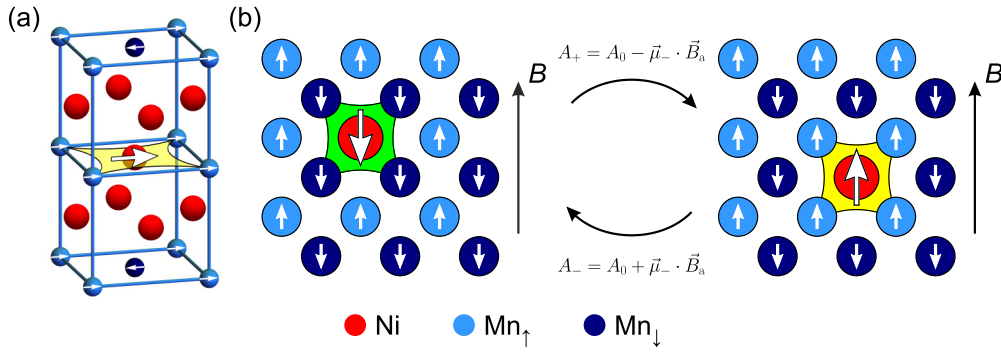|	Site-resolved μ (μ_B)								
	Mn_1	Mn_2	Mn_3	Mn_4	Mn_5	Mn_6	Ni_1	Ni_2	$\mu_{Total}(\mu_B)$
without excess Ni	−3.14	−3.14	−3.14	−3.14	3.14	3.14		0.00	0.00
with excess Ni		−3.13	−3.17	−3.16	3.15	3.22	0.73	0.09	5.00

FIG. 9. (a) $L1_0$ NiMn crystal structure from Fig. 1. The arrows indicate the direction of the magnetic moments. The Mn-plane of interest is marked in yellow with a Ni-excess-atom in the middle. (b) Schematic representation ("top view") of the biased diffusion of excess Ni in the Mn-plane due to an external applied magnetic field. The left state can be transformed into the right one and vice versa by simply moving the Ni by one atom. A_- and A_+ are the respective activation energies of these diffusion jumps. Here only the final states are shown, and no diffusion mechanism is specified.

Equation (9) implies that lower temperatures during annealing result in an increased pinned magnetization. While this is true for the equilibrium state, one has to consider the increased annealing-time at lower temperatures, which is not experimentally feasible.

At this point, the mentioned difference between the magnetic moment during diffusion, $\vec{\mu}_-$, and in a defect-free lattice, $\vec{\mu}_{\text{Total}}$, becomes important. While $\vec{\mu}_-$ has to be used to calculate the ratio $\tilde{N}$, the magnetic moment of the defect-free lattice $\vec{\mu}_{\text{Total}}$ is needed to calculate a mass magnetization from this ratio. Diffusion through vacancies is an example for this. It means that the Ni-atom can only swap positions with a nearest-neighbor vacancy. The vacancy itself removes a Mn-moment, which would have pointed in the same direction as the Ni-moment so that it will reduce μ_- compared to μ_{Total} during diffusion.

F. Polycrystalline materials

For a polycrystalline sample, the ratio of the occupation states $\tilde{N}_{\text{poly}}$ has to be determined by integrating the ratio of Eqs. (7a) and (7a) and on the surface of a unit hemisphere to simulate an equal abundance of every possible crystalline direction such that

$$\tilde{N}_{\text{poly}} = \frac{\frac{1}{2\pi} \int_0^{\frac{\pi}{2}} \int_{-\pi}^{\pi} \frac{\tilde{N}(\theta, \phi)}{\tilde{N}(\theta, \phi) + 1} \sin(\theta) d\phi \, d\theta}{\frac{1}{2\pi} \int_0^{\frac{\pi}{2}} \int_{-\pi}^{\pi} \frac{1}{\tilde{N}(\theta, \phi) + 1} \sin(\theta) d\phi \, d\theta}. \quad (10)$$

Here, θ and ϕ are the angles of $\vec{\mu}_-$. Without loss of generality, $\vec{B}_a = (0, 0, B_a)$, which simplifies the integral to

$$\tilde{N}_{\text{poly}} = \frac{\int_0^{\frac{\pi}{2}} \frac{\exp(\gamma \cos(\theta))}{\exp(\gamma \cos(\theta)) + 1} \sin(\theta) d\theta}{\int_0^{\frac{\pi}{2}} \frac{1}{\exp(\gamma \cos(\theta)) + 1} \sin(\theta) d\theta}. \quad (11)$$

With the abbreviation

$$\gamma = \frac{2\mu_- B_a}{k_B T_a}, \quad (12)$$

this integral is solved as

$$\tilde{N}_{\text{poly}} = \frac{\ln\left(\frac{1}{2}[1 + \exp(\gamma)]\right)}{\gamma + \ln(2) - \ln(1 + \exp(\gamma))} \quad (13)$$

with the assumption that $\gamma \geqslant 0$. Now, Eqs. (7a)–(7c) can be expressed with $\tilde{N}_{\text{poly}}$. To determine the mass magnetization of the pinned magnetization of a polycrystal $M_{\text{shift}}^{\text{poly}}$, one needs again to solve an integral on the surface of the unit hemisphere. This time, the relative excess of Ni-atoms in one of the AF sublattices is needed, and therefore, Eq. (7c) has to be integrated, so that

$$M_{\text{shift}}^{\text{poly}} = \frac{C\mu_{\text{Total}}}{2\pi} \int_0^{\frac{\pi}{2}} \int_{-\pi}^{\pi} \frac{\tilde{N}(\theta, \phi) - 1}{\tilde{N}(\theta, \phi) + 1}$$

$$\times \hat{e}(\theta, \phi) \cdot \hat{e}(\hat{\theta}, \hat{\phi}) \sin(\theta) d\phi d\theta. \quad (14)$$

$\hat{\theta}$ and $\hat{\phi}$ are the angles of the unit vector in the measurement direction. In the simplest case, $\vec{B}_a = (0, 0, B_a)$ points parallel to the measurement direction, so that

$$M_{\text{shift}}^{\text{poly}} = C\mu_{\text{Total}} \int_0^{\frac{\pi}{2}} \frac{\exp(\gamma \cos(\theta)) - 1}{\exp(\gamma \cos(\theta)) + 1} \cos(\theta) \sin(\theta) d\theta$$

$$= C\mu_{\text{Total}} \int_0^{\frac{\pi}{2}} \tanh\left(\frac{\gamma}{2} \cos(\theta)\right) \cos(\theta) \sin(\theta) d\theta. \quad (15)$$

From this, $M_{\text{shift}}^{\text{poly}}$ can be calculated as

$$M_{\text{shift}}^{\text{poly}} = C\mu_{\text{Total}} \frac{\pi^2 - 3\gamma^2 + 12\gamma \ln(1 + \exp(\gamma)) + 12\text{Li}_2(-\exp(\gamma))}{6\gamma^2}. \quad (16)$$

Here, Li_2 is the polylogarithm of order 2. We note that the pinned magnetization expected from a polycrystal is one-third of the single-crystal value for small values of γ, and then, with increasing γ, it approaches the expected value of half the single-crystal value.

V. DISCUSSION

We first compare our results with those reached in Ref. [10]. Using similar assumptions to ours, the authors determined relationships for the pinned magnetization in single-crystalline and polycrystalline NiMn. As it turns out, these relationships are the first-order Taylor series expansions of Eqs. (9) and (16), and they are therefore valid for small values of $2\mu_- B_a / k_B T_a$, which is the case for normal experimental conditions. The authors do not report a quantitative comparison between model and experiment.

Another observation the authors report is the appearance of an isotropic magnetization, which was thought to come from impurities in the sample, most likely an fcc Ni-rich Ni-Mn component. In the present study, we are able to confirm this assumption and locate these impurities within the surface region. The mechanism leading to the formation of Ni-rich Ni-Mn is the oxidation of Mn at the surface leaving a Ni-rich Ni-Mn subsurface layer. Polishing the surface removes MnO and the Ni-rich Ni-Mn and thus also the isotropic magnetization.

Now, we calculate the pinned magnetization from Eqs. (9) and (16). For that we use the magnetic moment per Ni-excess atom $\mu_{\text{Total}} = 5\mu_B$ obtained from *ab initio* calculations for NiMn with excess Ni (see Table I). The maximum possible pinned magnetization is obtained if all Ni-excess atoms occupy only one of the two AF sublattices. For $\text{Ni}_{51.6}\text{Mn}_{48.4}$ this results in a value of $7.9 \, \text{A}\,\text{m}^2/\text{kg}$. For the maximum amount of 56% of Ni in off-stoichiometric NiMn, for which the $L1_0$ structure is still stable [14], this maximum magnetization is $29.4 \, \text{A}\,\text{m}^2/\text{kg}$. To reach these values, one has to anneal the sample infinitely long at low temperatures as implied by Eq. (9).

Now, we provide a quantitative comparison between the model we use and the experimental results shown in Fig. 5. In the experiment, the sample was annealed for 14.4 h at 650 K in 9 T, for which M_{shift} has saturated and reached equilibrium (Fig. 4). We use Eq. (16) to calculate the pinned magnetization of a polycrystal. First, we assume that $\mu_- = \mu_{\text{Total}}$. This gives a total calculated magnetization of $0.12 \, \text{A}\,\text{m}^2/\text{kg}$, which is two orders of magnitude larger than the measured value of $(4.3 \pm 0.7) \times 10^{-3} \, \text{A}\,\text{m}^2/\text{kg}$.

One reason for this overestimation is possibly due to different diffusion mechanisms, which lead to a change in μ_-. If diffusion is mediated through monovacancies, then the vacancy itself replaces another Mn-moment from the lattice and reduces μ_- compared to μ_{Total}. μ_- is then only the moment of the additional Ni-atom, which is calculated to be $0.73\mu_B$. If μ_{Total} is then again assumed to be $5\mu_B$, Eq. (16) results in a total magnetization of $1.78 \times 10^{-2} \, \text{A}\,\text{m}^2/\text{kg}$, which is still four times larger than the measured value of $(4.3 \pm 0.7) \times 10^{-3} \, \text{A}\,\text{m}^2/\text{kg}$. To reach this value, μ_- would have to be $0.18\mu_B$.

VI. CONCLUSIONS

Annealing NiMn with excess Ni in an external field leads to a vertical shift in the magnetic field dependent magnetization curve. This shift originates from an imbalance of excess Ni atoms on Mn sites. Due to the magnetic field applied during annealing, one of the AF sublattices becomes energetically more favorable for the excess Ni atoms to occupy [10]. We confirm this with the results of *ab initio* calculations. However, in a quantitative comparison with experimental results, theory gives an overestimation for the pinned magnetization.

To be able to reach these conclusions with experimental support, it is important to eliminate any effect arising from those other than the pinned magnetization. We find these to be effects located at the surface and subsurface, which lead to additional magnetization arising from the occurrence of MnO and Ni-rich FM Ni-Mn.

APPENDIX: FIRST-PRINCIPLES CALCULATIONS

1. Coherent potential approximation

In the case of the coherent potential approximation (CPA), chemical disorder is modeled analytically. Calculations were performed with the help of the Korringa-Kohn-Rostoker (KKR) approach as implemented in the Munich SPR-KKR code [19,20] in the framework of the atomic sphere approximation (ASA) together with scalar relativistic corrections. The angular momentum expansion was carried out up to $l_{\text{max}} = 3$ (f-states). The electronic self-consistency was assumed to be reached when the error in the potential functions dropped below 10^{-5}. Brillouin zone integration was carried out using the special point method with a k-point grid of 15 points, which corresponds to a $17 \times 17 \times 12$ mesh in the full Brillouin zone.

To take into account systematically the effect of Ni excess on the magnetic properties, instead of equiatomic NiMn, we modeled near-equiatomic composition with slight Ni-excess on the Mn site in the middle of the cell [Mn_1 in Fig. 10(a)]. This allows us not to exclude completely Ni_1 interactions and evaluate the influence of Ni excess on the exchange parameters. For the same purpose, we modeled also the intermediate composition with equal Ni and Mn concentration in the central site (0.5, 0.5, 0.5) of the cell. Thus, further, we will discuss the results of CPA calculations performed for Ni-concentrations of 50.0625 at. %, (near-equiatomic NiMn), 53.125 at. %, and 56.1875 at. %.
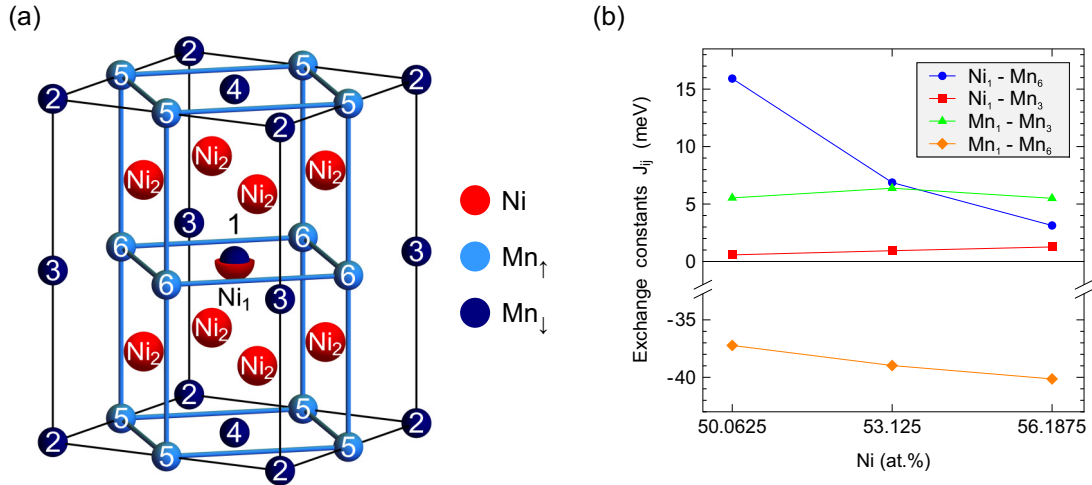
FIG. 10. (a) NiMn cell used in *ab initio* calculations with CPA approach. Antiparallel orientation of Mn magnetic moments forms layered AF configuration. (b) The dependence of exchange constants J_{ij} of the interacting atoms i and i on Ni-excess concentration. $J_{ij} > 0$ correspond to FM exchange, while $J_{ij} < 0$ are assigned to AF interaction. Numbering of atoms corresponds to the computational cell depicted on the left.

For the above-mentioned compositions, we performed calculations of the total energies, spin and orbital magnetic moments, and exchange constants. The exchange parameters J_{ij} define the interactions between pairs of atoms i and j of all different chemical types and positions as a function of the distance r_{ij} between them in terms of a classical Heisenberg model Hamiltonian

$$\mathcal{H}_{\mathrm{mag}} = -\sum_{i \neq j} J_{ij} \, \vec{e}_i \cdot \vec{e}_j,$$

where $\vec{e}_i$ and $\vec{e}_j$ describe the unit vectors of the orientation of the magnetic spin moments at sites i and j.

Total energy calculations for the [001], [100], and [110] spin moment directions showed that [110] is slightly more favorable than the other two. Thus, further discussion is presented for this case. Calculated spin (μ_s) and orbital (μ_l) magnetic moments for different Ni-excess concentrations are summarized in Table II. On the whole, AF NiMn becomes FM with introducing Ni on the Mn site. Ni atoms in their own sublattice (Ni$_2$), which are nonmagnetic in the stoichiometric composition, acquire spin and orbital magnetic moments with introducing Ni-excess. Contrary to this, spin magnetic moments of extra Ni (Ni$_1$) decrease by ≈ 1.7 times. The main question was the orientation of the Ni-excess magnetic moment in the Mn plane. Our calculations show that the magnetic moment of the Ni-excess atom (Ni$_1$) aligns parallel to the ones of nearest neighbor Mn$_6$ atoms and of Ni atoms in their planes

(Ni$_2$). Introducing Ni-excess results also in a slight decrease in μ_s of Mn$_1$ located at the center of the cell and Mn$_2$ due to the weakening AF Mn$_1$ − Mn$_2$ and FM Mn$_1$ − Mn$_1$ exchange interaction. The FM Ni$_1$ − Mn$_6$ exchange [blue circles in Fig. 10(b)] in near-equiatomic composition decreases by five times when Mn$_1$ is (almost) fully replaced by Ni, which leads to a decrease in $\mu_s^{\mathrm{Ni}_1}$.

We also calculated the magnetocrystalline anisotropy energy (MAE) in terms of the total energy difference between two spin moment directions [34–37] as MAE $= E_{\mathrm{tot}}^{110} - E_{\mathrm{tot}}^{001}$. The results of MAE calculations are presented in the last column of Table II. The obtained MAE $= -0.154$ meV/f.u. of near-equiatomic NiMn agrees with the earlier theoretical study of Sakuma [8]. Introducing Ni-excess increases anisotropy of the system, and the MAE becomes slightly larger in absolute value. The MAE values obtained in calculations for stoichiometric and Ni-excess NiMn are comparable with MAE for Ni$_2$MnGa [36,38].

2. Supercell approach

Supercell calculations were performed with the help of the Vienna *Ab Initio* Simulation Package (VASP) [21,22]. The exchange-correlation functional was treated within the generalized gradient approximation (GGA) following the Perdew, Burke, and Ernzerhof (PBE) scheme [23]. The energy cutoff for the plane-wave basis set were set to 460 eV. The calculations converged with an energy accuracy of

TABLE II. Site-resolved (in μ_B/atom) and total (in μ_B/Ni-excess-atom) spin magnetic moments μ_s and total orbital magnetic moments μ_l as well as MAE $= E^{110} - E^{001}$ (in meV/f.u.) of Ni$_{50+x}$Mn$_{50-x}$. Numbering of atoms corresponds to Fig. 10(a).

| Ni (at.%) | Site-resolved μ_s (μ_B) | | | | | | | | μ_s^{Total} (μ_B) | μ_l^{Total} (μ_B) | MAE |
	Mn$_1$	Mn$_2$	Mn$_3$	Mn$_4$	Mn$_5$	Mn$_6$	Ni$_1$	Ni$_2$			
50.0625	−3.31	−3.31	−3.31	−3.31	3.30	3.30	0.85	0.01	4.13	0.13	−0.154
53.125	−3.21	−3.26	−3.30	−3.30	3.27	3.31	0.64	0.05	4.83	0.08	−0.259
56.1875	−3.12	−3.21	−3.28	−3.28	3.24	3.32	0.50	0.13	4.91	0.08	−0.190

10^{-8} eV/atom. The Brillouin zone integration was performed with the first-order Methfessel-Paxton method using uniform Monkhorst-Pack $4 \times 4 \times 4$ k-point grid.

Modeling was performed for two structures. First, we modeled a 432-atom supercell of ideal NiMn by elongation of 16-atom cell with layered AF ordering by $3 \times 3 \times 3$. Secondly, we replace one Mn in the middle of the supercell [site (0.5; 0.5; 0.5)] by a Ni atom. Structures used in modeling as well as the results of supercell calculations and their discussion are presented in the main text of the paper.

[1] K. Takano, R. H. Kodama, A. E. Berkowitz, W. Cao, and G. Thomas, Interfacial Uncompensated Antiferromagnetic Spins: Role in Unidirectional Anisotropy in Polycrystalline Ni$_{81}$Fe$_{19}$/CoO Bilayers, Phys. Rev. Lett. **79**, 1130 (1997).

[2] J. Nogués, C. Leighton, and I. K. Schuller, Correlation between antiferromagnetic interface coupling and positive exchange bias, Phys. Rev. B **61**, 1315 (2000).

[3] U. Nowak, K. D. Usadel, J. Keller, P. Miltényi, B. Beschoten, and G. Güntherodt, Domain state model for exchange bias. I. Theory, Phys. Rev. B **66**, 014430 (2002).

[4] J. Keller, P. Miltényi, B. Beschoten, G. Güntherodt, U. Nowak, and K. D. Usadel, Domain state model for exchange bias. II. Experiments, Phys. Rev. B **66**, 014431 (2002).

[5] C. C. Wan, A. B. Harris, and D. Kumar, Heisenberg antiferromagnet with a low concentration of static defects, Phys. Rev. B **48**, 1036 (1993).

[6] N. Fujita, S. Kosugi, Y. Saitoh, Y. Kaneta, K. Kume, T. Batchuluun, N. Ishikawa, T. Matsui, and A. Iwase, Magnetic states controlled by energetic ion irradiation in FeRh thin films, J. Appl. Phys. **107**, 09E302 (2010).

[7] E. Krén, E. Nagy, I. Nagy, L. Pál, and P. Szabó, Structures and phase transformations in the Mn-Ni system near equiatomic concentration, J. Phys. Chem. Solids **29**, 101 (1968).

[8] A. Sakuma, Electronic structures and magnetism of CuAu-type MnNi and MnGa, J. Magn. Magn. Mater. **187**, 105 (1998).

[9] A. Berkowitz and K. Takano, Exchange anisotropy - a review, J. Magn. Magn. Mater. **200**, 552 (1999).

[10] L. Pál, T. Tarnóczi, and G. Konczos, Magnetic susceptibility anomaly in nearly equiatomic MnNi alloys, Physica Status Solidi B **42**, 49 (1970).

[11] W. H. Meiklejohn and C. P. Bean, New magnetic anisotropy, Phys. Rev. **102**, 1413 (1956).

[12] H. Ohldag, A. Scholl, F. Nolting, E. Arenholz, S. Maat, A. T. Young, M. Carey, and J. Stöhr, Correlation between Exchange Bias and Pinned Interfacial Spins, Phys. Rev. Lett. **91**, 017203 (2003).

[13] J. Guo, X. Zhao, Z. Lu, P. Shi, Y. Tian, Y. Chen, S. Yan, L. Bai, and M. Harder, Evidence for linear dependence of exchange bias on pinned uncompensated spins in an Fe/FeO bilayer, Phys. Rev. B **103**, 054413 (2021).

[14] M. Hansen, *Constitution of Binary Alloys, Materials Science and Engineering Series* (McGraw-Hill Book INC, New York, 1958).

[15] K. Adachi and C. Wayman, Transformation behavior of nearly stoichiometric Ni-Mn alloys, Metall. Trans. A **16**, 1567 (1985).

[16] J. Kasper and J. Kouvel, The antiferromagnetic structure of NiMn, J. Phys. Chem. Solids **11**, 231 (1959).

[17] D. Spisak and J. Hafner, Electronic and magnetic structure of Mn-Ni alloys in two and three dimensions, J. Phys.: Condens. Matter **11**, 6359 (1999).

[18] C. Gao, Spin structure of antiferromagnetic thin films investigated with spin-polarized scanning tunneling microscopy, Ph.D. thesis, Martin-Luther-Universität Halle-Wittenberg, 2006.

[19] H. Ebert, A spin polarized relativistic Korringa-Kohn-Rostoker (SPR-KKR) code for Calculating Solid State Properties, version 7.7, https://www.ebert.cup.uni-muenchen.de/index.php/en/software-en/13-sprkkr.

[20] H. Ebert, D. Koedderitzsch, and J. Minar, Calculating condensed matter properties using the KKR-Green's function method-recent developments and applications, Rep. Prog. Phys. **74**, 096501 (2011).

[21] G. Kresse and J. Furthmüller, Efficient iterative schemes for ab initio total-energy calculations using a plane-wave basis set, Phys. Rev. B **54**, 11169 (1996).

[22] G. Kresse and D. Joubert, From ultrasoft pseudopotentials to the projector augmented-wave method, Phys. Rev. B **59**, 1758 (1999).

[23] J. P. Perdew, K. Burke, and M. Ernzerhof, Generalized Gradient Approximation Made Simple, Phys. Rev. Lett. **77**, 3865 (1996).

[24] M. Siewert, Electronic, magnetic and thermodynamic properties of magnetic shape memory alloys from first principles, Ph.D. thesis, University of Duisburg-Essen, 2012.

[25] P. Entel, M. E. Gruner, M. Acet, A. Çakır, R. Arróyave, T. Duong, S. Sahoo, S. Fähler, and V. V. Sokolovskiy, Properties and decomposition of Heusler alloys, Energy Technol. **6**, 1478 (2018).

[26] V. Petříček, M. Dušek, and L. Palatinus, Crystallographic computing system JANA2006: General features, Z. Krist.-Cryst. Mater. **229**, 345 (2014).

[27] L. Pál, E. Krén, G. Kádár, P. Szabó, and T. Tarnóczi, Magnetic structures and phase transformations in Mn-based CuAu-I type alloys, J. Appl. Phys. **39**, 538 (1968).

[28] M. Ghosh, K. Biswas, A. Sundaresan, and C. Rao, MnO and NiO nanoparticles: Synthesis and magnetic properties, J. Mater. Chem. **16**, 106 (2006).

[29] K. v. Buschow, P. Van Engen, and R. Jongebreur, Magneto-optical properties of metallic ferromagnetic materials, J. Magn. Magn. Mater. **38**, 1 (1983).

[30] S. Kaya and A. Kussmann, Ferromagnetismus und Phasengestaltung im Zweistoffsystem Nickel-Mangan, Z. Phys. **72**, 293 (1931).

[31] C. Wert, Diffusion coefficient of C in α-iron, Phys. Rev. **79**, 601 (1950).

[32] Z. Balogh and G. Schmitz, Diffusion in metals and alloys, in *Physical Metallurgy* (Elsevier, Amsterdam, 2014), pp. 387–559.

[33] A. Aharoni *et al.*, *Introduction to the Theory of Ferromagnetism* (Clarendon, 2000), Vol. 109.

[34] J. Enkovaara, A. Ayuela, L. Nordström, and R. M. Nieminen, Magnetic anisotropy in Ni$_2$MnGa, Phys. Rev. B **65**, 134422 (2002).

[35] R. Umetsu, A. Sakuma, and K. Fukamichi, Magnetic anisotropy energy of antiferromagnetic L1$_0$-type equiatomic Mn alloys, Appl. Phys. Lett. **89**, 052504 (2006).

[36] M. E. Gruner, P. Entel, I. Opahle, and M. Richter, Ab initio investigation of twin boundary motion in the magnetic

shape memory Heusler alloy Ni$_2$MnGa, J. Mater. Sci. **43**, 3825 (2008).

[37] A. Edström, M. Werwiński, D. Iuşan, J. Rusz, O. Eriksson, K. P. Skokov, I. A. Radulov, S. Ener, M. D. Kuz'min, J. Hong, M. Fries, D. Y. Karpenkov, O. Gutfleisch, P. Toson, and J.

Fidler, Magnetic properties of (Fe$_{1-x}$Co$_x$)$_2$B alloys and the effect of doping by 5d elements, Phys. Rev. B **92**, 174413 (2015).

[38] H. C. Herper, Ni-based Heusler compounds: how to tune the magnetocrystalline anisotropy, Phys. Rev. B **98**, 014411 (2018).